Resonant acoustic nonlinearity and loss in additively manufactured stainless steel*

Ward L. Johnson[1,a)], Justin G. Whiting[2], Felix H. Kim[2], Paul R. Heyliger[3] and Nik W. Hrabe[1]

[1]*Applied Chemicals and Materials Division, National Institute of Standards and Technology, 325 Broadway St., Boulder, CO 80305*
[2]*Intelligent Systems Division, National Institute of Standards and Technology, 100 Bureau Dr., Gaithersburg, MD 20899*
[3]*Department of Civil and Environmental Engineering, Colorado State University, Fort Collins, CO 80523*

[a)]Corresponding author: wjohnson@boulder.nist.gov

Abstract. Resonant acoustic nonlinearity and loss in additively manufactured stainless steel were measured with the aim of assessing the potential of such measurements for nondestructively sensing defects that degrade mechanical performance. The material was fabricated by laser powder bed fusion (L-PBF) with intentional differences in spacing between laser tracks, which produced differences in porosity and amount of incompletely melted powder. The composition of the material was that of nominal 17-4 stainless steel. X-ray computed tomography was employed to image the structure of pores, including incompletely melted particles. Porosities were determined to be in the range of approximately 0.05 % to 11.9 % , and unmelted powder fractions were in the range of approximately 0 % to 2.3 %. Noncontacting electromagnetic-acoustic transduction was employed to excite the lowest-order cutoff torsional mode in cylindrical specimens. Resonant frequencies as a function of RF amplitude were determined through time-domain analysis of decaying waveforms following tone-burst excitation, and acoustic loss was determined from an exponential fit of amplitude *vs.* time. Resonant frequencies were found to decrease with time during ringdown, corresponding to an unusual positive dependence on vibrational amplitude. Amplitude-dependent frequency shifts and acoustic loss increased between specimens monotonically with porosity and unmelted powder fraction.

INTRODUCTION

Additive manufacturing (AM) of parts with laser- or electron-beam melting of metallic powder is widely recognized as offering, for many applications, a number of advantages relative to conventional metallurgical processes, including near-net-shape fabrication and a capability of generating innovative compositions and microstructures [1]. However, commercial adoption of additively manufactured parts is impeded by limitations on material validation, and these limitations are partly associated with an absence of broadly applicable techniques for nondestructively characterizing small-scale porosity and unmelted powder, which are typical features of AM materials with nonoptimal build parameters [2, 3]. While X-ray computed tomography (X-ray CT) is a powerful technique for three-dimensional imaging of porosity and morphology in AM materials, it is impractical for many parts because of limitations on X-ray penetration depth and associated image resolution [4, 5].

In this paper, we summarize an exploratory study of methods for sensing defects in post-process AM parts through resonance measurements of acoustic nonlinearity and anelasticity (loss). The focus on a resonance technique is motivated partly by the expectation that transduction and signal interpretation with complex AM geometries and microstructures will be more straightforward with resonance measurements than with acoustic pulse-echo measurements. Less access to surfaces of a part are required, signals are not made more complicated by nonplanar surfaces, and obscuration of defects by scattering from other defects is not an issue. Our specific focus on nonlinearity and loss is motivated by the fact that defect contributions to nonlinearity and loss are, in many materials, strongly correlated

with material degradation and eventual mechanical failure. From the practical perspective of nondestructive evaluation (NDE), measurements of nonlinearity and loss also offer the advantage of being relatively insensitive to small variations in specimen dimensions and ambient temperature, which directly affect uncertainties in measurements of linear elastic properties.

SPECIMENS

Specimens in this study were built by the laser powder bed fusion (L-PBF) method from nitrogen-atomized powder with a composition matching the nominal composition of 17-4 stainless steel. The laser had a power of 195 W and a scanning speed of 1000 mm/s. Hatch spacings between laser tracks were intentionally varied from 0.10 mm to 0.30 mm between parts to provide several levels of porosity. The built parts, after removal from the baseplate, had diameters of approximately 30 mm and lengths of approximately 9 mm. From each of these parts, smaller cylinders were cut by electrical discharge machining (EDM). The dimensions and hatch spacings of the specimens are listed in Table 1. Specimens labeled "A" or "B" with the same numerical index (1, 2, 3, or 4) were cut from the same build. The smaller specimens ("A") were used for X-ray CT measurements, because they provided higher image resolution. The larger specimens ("B") were used for acoustic resonance measurements, because they provided greater signal strength. Lengths of the specimens labeled "A" were not measured but were close to those listed in Table 1 for "B" specimens. As described below, only $\approx 28\,\%$ of each specimen's length was included in the X-ray CT measurements.

TABLE 1. Specimen labels, laser hatch spacing, and specimen dimensions. Uncertainties in length are 0.002 mm (one standard deviation of the measurements). Uncertainties in diameter are 0.05 mm, not including an axially oriented ridge on one side of each specimen that is an artifact of the wire-EDM cutting.

Specimen label	Hatch spacing (mm)	diameter (mm)	ridge height (mm)	length (mm)
1A	0.10	2.995	0.128 ± 0.006	
1B	0.10	10.006	0.019 ± 0.006	9.140
2A	0.15	2.999	0.114 ± 0.006	
2B	0.15	9.993	0.085 ± 0.006	9.140
3A	0.20	2.996	0.11 ± 0.01	
3B	0.20	10.003	0.032 ± 0.006	9.141
4A	0.30	2.999	0.148 ± 0.003	
4B	0.30	10.005	0.05 ± 0.01	9.147

EXPERIMENTAL METHODS

X-ray CT

The internal structure of specimens was evaluated using an X-ray CT system (Zeiss Xradia 500[1]). A 3.0 μm voxel size (edge length) was achieved. The 399 slices of the data sets were first cropped to a cylindrical volume (848 voxel diameter x 399 voxel height). The thresholding process was performed in the environment of VGStudioMax 3.2 (Volume Graphics)[1]. The cropped data were filtered using an adaptive Gaussian filter (smoothing coefficient = 0.8, edge threshold = 0.1). A local thresholding algorithm, VGEasyPore, was used to threshold the images. The local contrast threshold was found based on a technique described by Kim *et al.* [6]. Initial thresholded images were further refined with the local adaptive thresholding algorithm of VGStudioMax 3.2. Figs. 1 (a) and (b) illustrate the effect of this thresholding algorithm applied to a section of an image from specimen 3A.

To remove the contributions of partially melted powder (particle-like features in the images), a sequence of image-processing algorithms was applied in the environment of Avizo 9.5.0 (ThermoFischer Scientific)[1]. The holes of the pores phases were filled, and then a morphological closing operation was applied. This process removed the majority of visibly identifiable partially melted particles without significantly changing the general pore shape and boundaries, as illustrated in Fig. 1 (c). The porosity from the resultant image stack minus the porosity before removal of powder yielded the unmelted powder fraction.

[1] Identification of this commercial product is provided for technical completeness and does not reflect an endorsement by NIST.

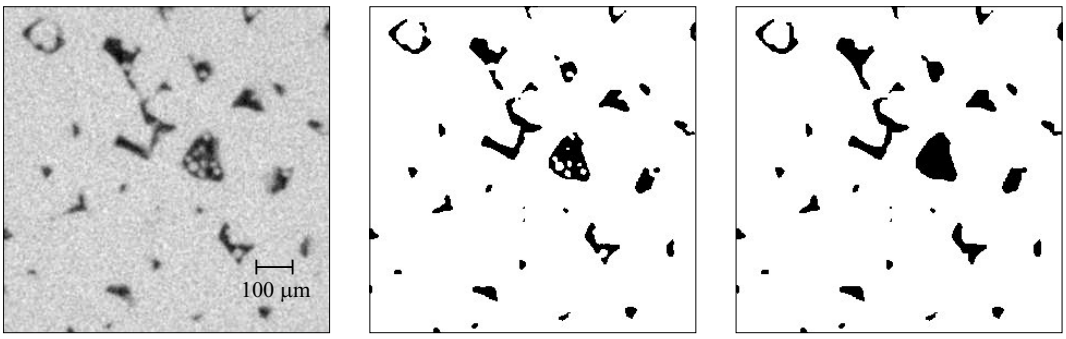

FIGURE 1. Section of an X-ray CT image slice from specimen 3A, illustrating the steps in image processing: (a) original grayscale image, (b) thresholded image, and (c) thresholded image with partially melted powder removed.

Resonant Ultrasonics

An electromagnetic-acoustic-resonance (EMAR) technique involving Lorentz coupling was employed to excite and detect vibrations in the specimens. As illustrated in Fig. 2, a gated amplifier (RITEC RAM-5000 SNAP[1]) was used to provide radio-frequency (RF) tone bursts with frequencies in the range of 426 kHz to 496 kHz and a repetition rate of 2 Hz. The duration of tone bursts was 4.6 ms for specimens 1B, 2B, and 3B and 1.5 ms for 4B. Burst amplitudes were approximately 141 V for 1B, 2B, and 3B, and 181 V for 4B.

The output of the gated amplifier was passed through an active diplexer to a coil that surrounded a specimen. A static magnetic field B with a magnitude of (0.540 ± 0.005) T was oriented perpendicular to the axis of the coil. This field was produced by a Halbach magnet. As shown in Fig. 2, the cylindrical axis of the specimen was perpendicular to the direction of the magnetic field and the axis of the coil.

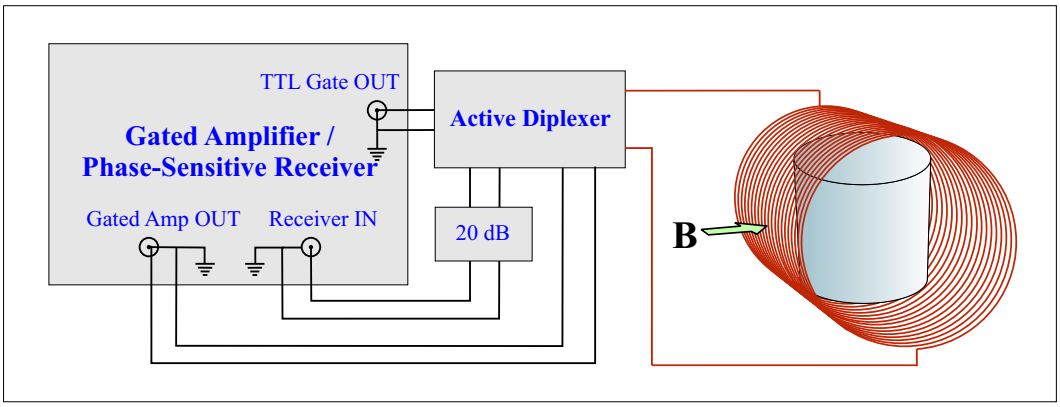

FIGURE 2. Block diagram of the electronic system, EMAR coil, and specimen (not to scale).

With the configuration of the coil and specimen in Fig. 2, oscillating currents in the coil induce eddy currents in opposite directions on the cylindrical sides of the specimen close to the coil and in directions perpendicular to the coil axis on the top and bottom on the specimen. The cross product of these currents and B leads primarily to azimuthal forces on the cylindrical sides of the specimen closest to the coil. These forces selectively couple to torsional modes of the specimen with no phase variation along the length (*i.e.*,"cutoff" torsional modes with only radial phase variation [7]). To our knowledge, this EMAR configuration for exciting torsional modes was not employed in any previous published studies. The present study is focused on the lowest-order cutoff torsional mode. The frequency f of this mode at cutoff, under the approximation of transverse elastic isotropy, is given by [7, 8].

$$f = \frac{5.13562\, v_s}{2\pi a}, \tag{1}$$

where v_s is the shear velocity and a is the cylinder radius.

Resonant RF signals during free decay ("ringdown") after tone-burst excitation were passed to the receiver of the RITEC system and then to phase-detector modules within this instrument to extract the time-dependent amplitudes of the in-phase and out-of-phase components of the signal, relative to the reference driving sinusoid that was gated to generate the tone burst. These components were digitized and passed to a computer.

The acquired waveforms were corrected for nonlinearity of the receiver and relative differences in gain of the two phase-detector channels. Also, time-dependent electronic offsets of the phase-detector voltages following a tone burst in the absence of an acoustic resonance were subtracted from the resonant waveforms. These voltage offsets were found to be ≈ 1 % (or less) of the phase-detector voltages from the resonant signal.

As described elsewhere [9], the measured in-phase and out-of-phase components give, after compensation for receiver nonlinearity and time-dependent baselines, the time-dependent amplitude $A(t)$ and phase $\phi(t)$ of the RF voltage on the coil relative to the reference sinusoid:

$$A(t) = \frac{(PhDet1^2 + PhDet2^2)^{1/2}}{(\text{receiver gain})(\text{preamp gain})}, \tag{2}$$

$$\phi(t) = \arctan(PhDet2/PhDet1), \tag{3}$$

where $PhDet1$ and $PhDet2$ are, respectively, the in-phase and out-of-phase waveforms from the RITEC system, and t is time. $A(t)$ is proportional to the vibrational amplitude of the specimen.

Apart from any time-dependent drift or noise in resonant frequency, phase, or reference frequency associated with temperature, electronics, or external perturbations, the instantaneous resonant frequency $f(t)$ during ringdown is given by [10]

$$f(t) = \frac{1}{2\pi}\frac{d\phi}{dt} + f_{ref}, \tag{4}$$

where f_{ref} is the frequency of the reference sinusoid, which is constant during a given ringdown. Acoustic loss Q^{-1} is determined from an exponential fit of RF amplitude during ringdown.

RESULTS

X-ray CT

Typical X-ray CT image slices from specimens 1A, 2A, 3A, and 4A are shown in Fig. 3. These images show porosity increasing with greater hatch spacing. In specimens 3A and 4A, evidence for individual scan tracks can be seen, with relative orientations matching the 66.6 ° rotation setting of the L-PBF system. Unmelted powder is visible on the scale of these images within some pores of specimens 3A and 4A.

Table 2 lists volume fractions of porosity and unmelted powder determined from X-ray CT on the four specimens. No unmelted powder was found in specimen 1A, which had build parameters matching those recommended by the L-PBF manufacturer for 17-4 stainless steel. The uncertainties in Table 2 only include effects associated with variations in input parameters for the local-contrast thresholding algorithm. They do not include potential systematic effects, such as lack of detection of pores with dimensions below the resolution limit or intrinsic bias in quantifying partial volumes of pores within few voxels.

TABLE 2. Volume fractions of porosity and unmelted powder determined from X-ray CT on four specimens.

Specimen	Porosity (%)	Unmelted powder (%)
1A	0.050 ± 0.006	0.000 (+ 0.008 / - 0.000)
2A	1.37 ± 0.046	0.08 ± 0.066
3A	4.25 ± 0.09	0.51 ± 0.12
4A	11.91 ± 0.34	2.28 ± 0.54

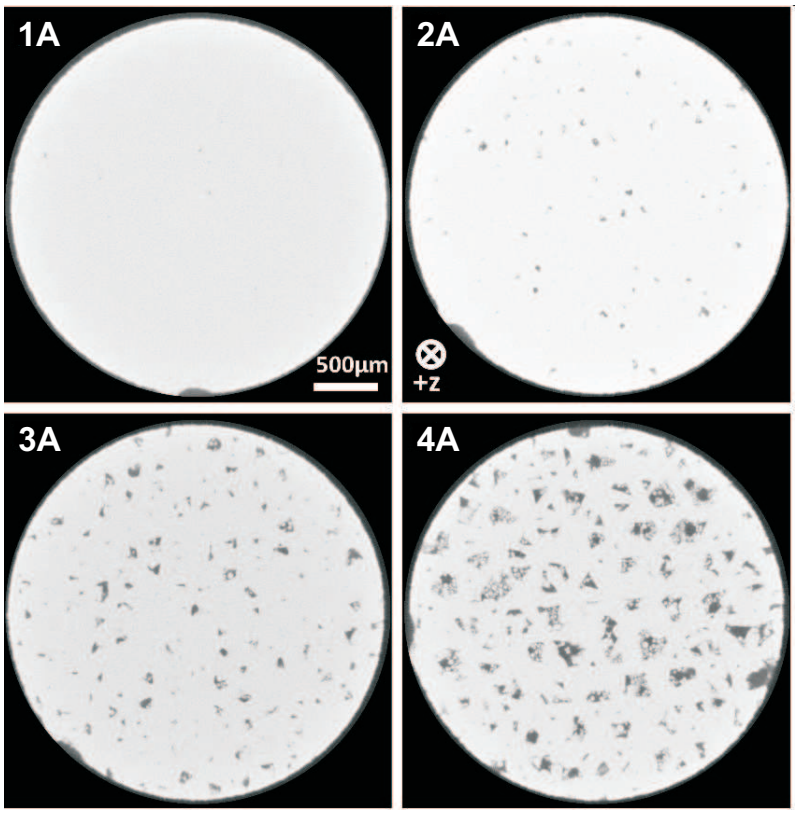

FIGURE 3. Raw X-ray CT image slices from specimens 1A, 2A, 3A, and 4A.

Acoustic Measurements

Fig. 4 shows values of RF amplitude and phase measured during resonant ringdown of specimen 2B after reaching approximate thermal equilibrium under acoustic excitation. These values were obtained through a multi-step algorithm involving waveform averaging, background subtraction, and correction for receiver nonlinearity, which is described in the Appendix. The zero for t in Fig. 4 is 1 ms after the end of the toneburst.

The amplitude dependence of the resonant frequency was determined from the data in Fig. 4 by, first, fitting the measured ϕ *vs.* t to a fourth order polynomial. This fit is plotted as the smooth curve in Fig. 4(b). The time derivative of the polynomial fit and the average drive frequency were inserted into Eq. 4 to obtain the time-dependent resonant frequency $f(t)$. These values were then expressed as fractional changes in frequency relative to the frequency $f_{1.5}$ at an RF amplitude $A(t)$ of 1.5 mV during the ringdown. This translation of the results to relative values during ringdown is required for a comparison of values obtained from the different specimens, which have different resonant frequencies. Also note that, when expressed as fractional shifts, the results are also not affected by differences in drive frequency of data sets that were averaged to produce $A(t)$ and $\phi(t)$. (See Appendix.) The choice of 1.5 mV for the reference amplitude is somewhat arbitrary but is associated with the fact that results were found to be more reproducible when referenced to an amplitude substantially greater than the background noise level. Fractional shifts in frequency, $(f(t) - f_{1.5})/f_{1.5}$, from the data in Figs. 4 are plotted *vs.* corresponding $A(t)$ in Fig. 5(a).

The data in Fig. 5(a) are repeated in Fig. 5(b) along with 15 additional sets of data from this specimen, 16 sets of data from 1B, and 6 sets of data from 3B. Note that the results for 3B in Fig. 5 are plotted on the right scale, which has a range five times greater than that of the left scale that is used for 1B and 2B. Nonlinear measurements on specimen 4B were found to be impractical due to interference from another acoustic mode.

Partial statistical analysis of the data in Fig. 5(b) is pursued by considering fractional shifts in frequency at $A(t) = 3.0$ mV relative to $f_{1.5}$. Table 3 lists the mean values and standard deviations of $(f_{3.0} - f_{1.5})/f_{1.5}$ for specimens 1B, 2B, and 3B, along with data on Q^{-1} from all of the specimens.

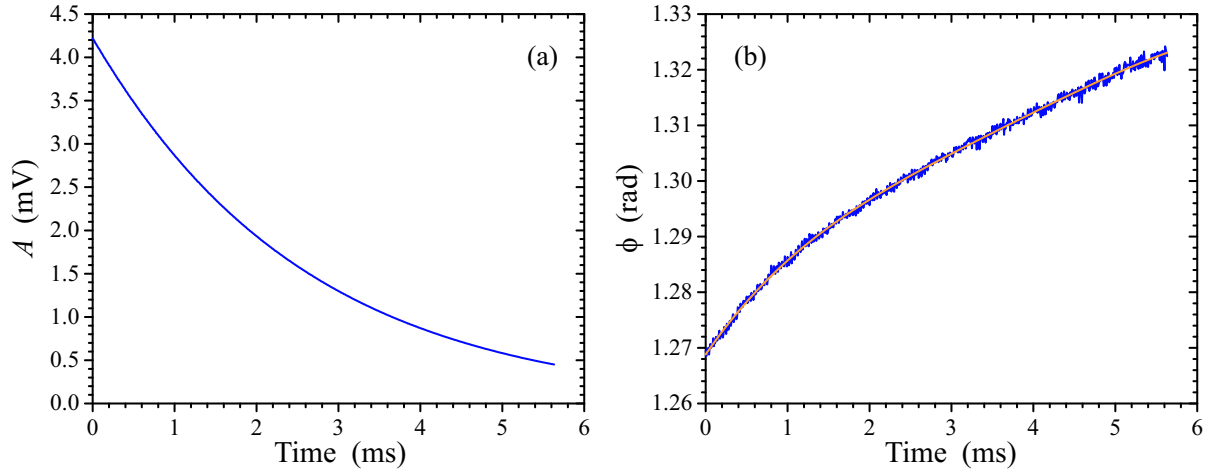

FIGURE 4. (a) RF amplitude $A(t)$ on the coil and (b) phase $\phi(t)$ *vs* ringdown time t calculated from waveforms $PhDet1(t)$ and $PhDet2(t)$ from specimen 2B through the use of Eqs. 2 and 3. The smooth line in (b) is a least-squares fit of ϕ *vs.* t to a fourth-order polynomial.

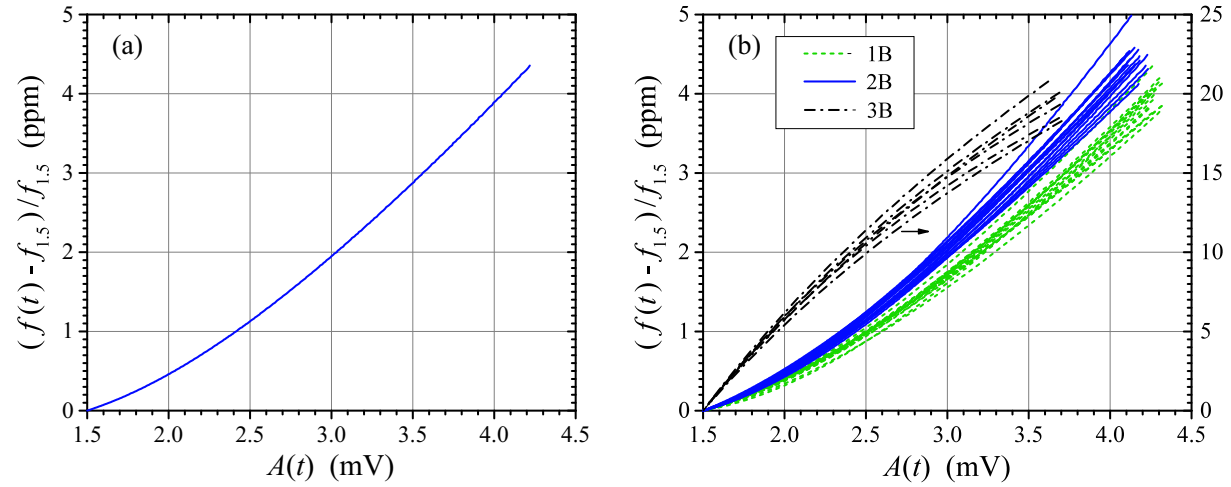

FIGURE 5. $(f(t) - f_{1.5})/f_{1.5}$ *vs.* $A(t)$ calculated from (a) the data from specimen 2B shown in Fig. 4 and (b) all data from 1B, 2B, and 3B. Data from 1B and 2B are plotted on the left scale of (b), and those from 3B are plotted on the right scale.

The distributions of measurements of fractional frequency shifts of 1B and 2B overlap within three standard deviations of the means listed in Table 3. However, a two-sample t-test of the measured values of $(f_{3.0} - f_{1.5})/f_{1.5}$ for 1B and 2B (16 values for each specimen) found that the mean for 2B is significantly greater than that for 1B, with a p-value of 4.1×10^{-15} if equal variance is assumed and a p-value of 2.7×10^{-14} if equal variance is not assumed. The difference between mean measured values of Q^{-1} of all of the specimens (summarized in Table 3) is also found to be statistically highly significant.

Figure 6 shows mean fractional frequency shifts and Q^{-1} from Table 3 plotted *vs.* (a) porosity and (b) unmelted powder fraction with the means of specimen 1B subtracted. Since the level of porosity in specimen 1B is an order of magnitude smaller than that of 2B and no unmelted powder was detected in 1B, the ordinate in Fig. 6 is an approximate measure of the contributions of pores and/or unmelted powder to nonlinearity and loss.

TABLE 3. Mean values of $f_{1.5}$ (resonant frequency at $A(t)$ = 1.5 mV during ringdown) and mean values and standard deviations of $(f_{3.0} - f_{1.5})/f_{1.5}$ and Q^{-1} from the data represented in Fig. 5(b), where $f_{3.0}$ is the resonant frequency at $A(t)$ = 3.0 mV. Values of $f_{1.5}$ for each specimen varied by approximately ± 50 Hz between experiments.

Specimen	$f_{1.5}$ (kHz)	Mean $(f_{3.0} - f_{1.5})/f_{1.5}$ (ppm)	Standard deviation of $(f_{3.0} - f_{1.5})/f_{1.5}$ (ppm)	Mean Q^{-1} (10^{-4})	Standard deviation of Q^{-1} (10^{-4})
1B	495.9	1.69	0.06	2.47	0.01
2B	486.2	2.04	0.08	2.59	0.01
3B	471.5	14.7	0.7	3.118	0.009
4B	426.5			43	3

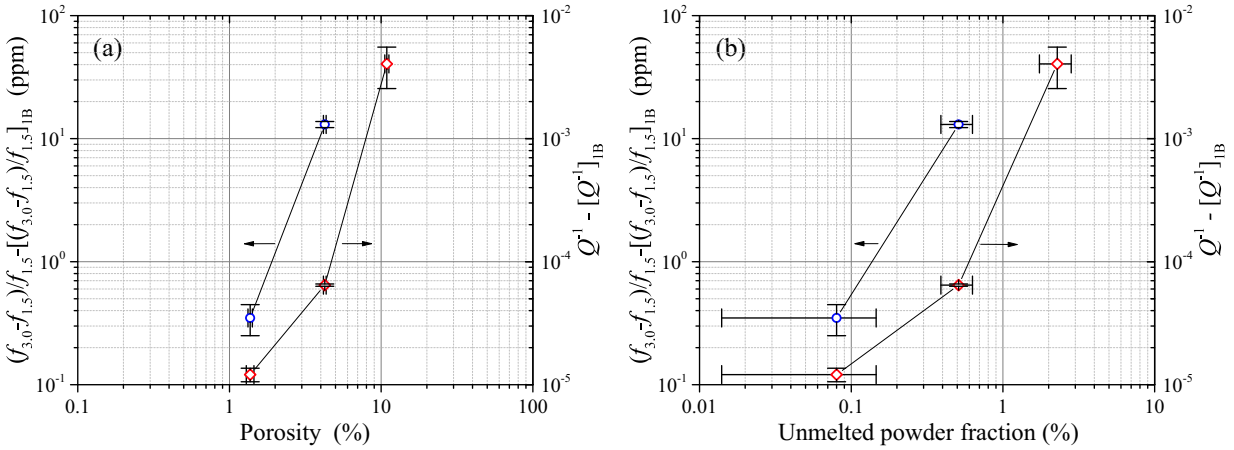

FIGURE 6. Mean fractional frequency shifts and Q^{-1} plotted *vs.* (a) porosity and (b) unmelted powder fraction with the mean fractional frequency shift and Q^{-1} of specimen 1B subtracted.

DISCUSSION

The sign of the observed dependence of frequency on vibrational amplitude is unusual. A number of previous resonance studies of acoustic nonlinearity arising from cracks and other microstructual defects in various materials have reported decreases in resonant frequency and increases in Q^{-1} with increasing vibrational amplitude [11, 12, 13], and one of these studies employed a time-domain measurement technique similar to that in the present study [9]. Although positive nonlinear frequency shifts have been reported for some materials (*e.g.*, [14, 15]), we are not aware of any previous study that found a correlation of such shifts with defects in metals.

The observed shifts in frequency are not linearly dependent on vibrational amplitude (Fig. 5). This result is also unusual, but it is not unique in the literature [16, 17, 18]. The curvature of the plots in Fig. 5 indicates that the stress-strain relation involves terms higher than quadratic, which goes beyond the normal approximation employed in analysis of nonlinear acoustic measurements.

In comparing the results in this report with previous publications, it may also be useful to note that the analysis of frequency data in Fig. 5 indicates a resolution on the order of 0.1 ppm for the lower-porosity specimens 1B and 2B (Table 3). This value is two to three orders of magnitude smaller than that reported for nonlinear resonance ultrasound spectroscopy (NRUS) [12], which is the technique most extensively used to study resonant nonlinearity of materials. However, one cannot use these relative resolutions to directly compare the sensitivities of the two techniques to nonlinear terms in the stress-strain relation, because maximal vibrational amplitudes in NRUS are expected to be much greater than those generated by noncontacting transduction in the present study.

The data in Fig. 6 provide evidence that correlations of porosity and powder fraction with nonlinearity and loss in each of the specimens are substantially different. For example, Fig. 6 (a) shows the enhanced nonlinearity (relative to specimen 1B) as approximately proportional to the cube of the porosity, while Fig. 6 (b) shows it as approximately proportional to the square of the unmelted powder fraction. These differences are associated with the fact that the fractional differences in unmelted powder fraction had a greater-than-linear dependence on porosity (Table 3).

An exploration of physical effects that contribute to the results presented here is beyond the scope of this study. However, we note that some degree of stiffening of metals under increasing stress (including resonant vibrational stress) is predicted to occur as a result of stress dependence of the effective tension of dislocations in some orientations [19]. With respect to this potential contribution to bulk nonlinearity, we also note that the degree of melting of powder is expected to affect dislocation densities.

While nonlinearity and loss are the primary foci of this study, the results for resonant frequencies $f_{1.5}$ in Table 3 should also be noted. Specimens 2B, 3B, and 4B were found to have resonant frequencies that were, respectively, 2.0 %, 4.9 %, and 14 % less than that of specimen 1B, and these differences are two to three orders of magnitude greater than the standard deviations in the resonant frequency measurements. These fractional differences are, respectively, 1.5, 1.2, and 1.2 times the increases in porosity relative to that of specimen 1B. They are interpreted as primarily a linear elastic effect associated with differences in porosity [20, 21, 22], although small anelastic contributions also are expected from the measured differences in Q^{-1} [23].

CONCLUSIONS

The resonant frequencies of additively manufactured 17-4 stainless steel specimens were found to decrease monotonically during ringdown after tone-burst excitation, corresponding to a positive dependence of frequency on vibrational amplitude. The sign of these observed frequency shifts *vs.* amplitude is opposite to that reported in a number of previous studies of acoustic nonlinearity from cracks and other microstructural defects in various materials. The observed nonconstant slope of frequency *vs.* amplitude is also unusual (although not unprecedented) and indicates the presence of higher-than-quadratic terms in the stress-strain relation.

Acoustic nonlinearity and loss were found to increase monotonically with porosity and unmelted powder fraction. In particular, statistically significant differences were found between specimens 1B and 2B, and this result provides evidence for detection of effects arising from ≈ 1 % porosity and/or ≈ 0.1 % unmelted powder fraction. The physical mechanisms for the observed nonlinearity and loss have not been determined.

APPENDIX: WAVEFORM PROCESSING

Values of $A(t)$ and $\phi(t)$ were determined from raw phase-detector waveforms through a process involving averaging and correction for receiver nonlinearity and time-dependent background of phase-detector voltages. The example of data from specimen 2B in Fig. 4 was obtained by, first, acquiring raw phase-detector waveforms with a fixed excitation frequency near the torsional resonance ($\approx$ 486.2 kHz) over a period of 20 s and recording the average of these waveforms and the drive frequency. During this twenty-second acquisition period, temperature-related drift in the resonant frequency was less than 0.1 Hz (0.2 ppm). This process of acquiring an averaged waveform was repeated eight times. Between each twenty-second acquisition period, the drive frequency was adjusted for temperature-related drift in frequency through the use of a real-time algorithm that is described elsewhere [24]. Each of the eight averaged waveforms was then corrected for nonlinearity of the receiver and time-dependent backgrounds of the phase detectors to yield corrected values of $PhDet1(t)$ and $PhDet2(t)$. These values were inserted into Eqs. 2 and 3 to obtain $A(t)$ and $\phi(t)$ for each averaged waveform. Finally, the eight resultant sets of $A(t)$ and $\phi(t)$ were averaged to obtain the values shown in Fig. 4. The drive frequencies of the eight sets were also averaged.

REFERENCES

[1] I. Gibson, D. W. Rosen, and Brent Stucker, *Additive Manufacturing Technologies: 3D Printing, Rapid Prototyping, and Direct Digital Manufacturing* (Springer, New York, 2015).

[2] *Measurement Science Roadmap for Metal-Based Additive Manufacturing*, prepared by Energetics Inc., Columbia, MD, for NIST (2013), p. 19.

[3] M. Seifi, M. Gorelik, J. Waller, N. Hrabe, N. Shamsaei, S. Daniewicz, J. J. Lewandowski, *JOM*, **69**, pp. 439–455 (2017).

[4] J. P. Kruth, M. Bartscher, S. Carmignato, R. Schmitt, L. De Chiffre, A. Weckenmann, "Computed tomography for dimensional metrology," *CIRP Annals*, **60**, pp. 821–842 (2011).

[5] L. De Chiffre, S. Carmignato, J. P. Kruth, R. Schmitt, A. Weckenmann, "Industrial applications of computed tomography," *CIRP Annals*, **63**, pp. 655–677 (2014).

[6] F. H. Kim, S. P. Moylan, E. J. Garboczi, J. A. Slotwinski, "Investigation of pore structure in cobalt chrome additively manufactured parts using X-ray computed tomography and three-dimensional image analysis," *Additive Manufacturing*, **17**, pp. 23–38 (2017).

[7] W. L. Johnson, B. A. Auld, and G. A. Alers, "Spectroscopy of resonant torsional modes in cylindrical rods using electromagnetic-acoustic transduction," *J. Acoust. Soc. Am.*, **95**, pp. 1413–1418 (1994).

[8] S. V. Eringen and E. S. Şuhubi, *Elastodynamics* (Academic, New York, 1975), Vol. II.

[9] W. L. Johnson, S. A. Kim, G. S. White, J. Herzberger, K. L. Peterson, and P. R. Heyliger, "Time-domain analysis of resonant acoustic nonlinearity arising from cracks in multilayer ceramic capacitors," *AIP Conference Proceedings* **1706**, 060005, (2016).

[10] E. Rubiola, *Phase Noise and Frequency Stability in Oscillators* (Cambridge University Press, Cambridge, 2009), p. 6.

[11] K. E.-A. Van Den Abeele, A. Sutin, J. Carmeliet, and P. A. Johnson, "Micro-damage diagnostics using nonlinaer elastic wave spectroscopy," *NDT&E Int.*, **34**, pp. 239–248 (2001).

[12] S. Haupert, F. Renaud, J. Rivière, M. Talmant, P. A. Johnson, and P. Laugier, "High-accuracy acoustic detection of nonclassical component of material nonlinearity," *J. Acoust. Soc. Am.*, **130**, pp. 2654–2661 (2011).

[13] T. Ohtani, Y. Kusanagi, and Y. Ishii, "Noncontact nonlinear resonant ultrasound spectroscopy to evaluate creep damage in an austenitic stainless steel," *AIP Conference Proceedings* **1511**, pp. 1227–1233 (2013).

[14] H. Zhang, J. A. Kosinski, Y. Xie, and J. A. Turner, "Drive-Level Dependence of Doubly Rotated Langasite Resonators With Different Configurations," *IEEE Trans. Ultrason. Ferro. Freq. Ctrl.*, **60**, pp. 963–969 (2013).

[15] S. K. Chakrapani and D. J. Barnard, "Determination of acoustic nonlinearity parameter (β) using nonlinear resonance ultrasound spectroscopy: Theory and experiment," *J. Acoust. Soc. Am.*, **114**, pp. 919–928 (2017).

[16] V. E. Nazarov and A. B. Kolpakov, "Experimental investigations of nonlinear acoustic phenomena in polycrystalline zinc," *J. Acoust. Soc. Am.*, **107**, pp. 1915–1921 (2000).

[17] K. Winkler, A. Nur, and M. Gladwin, "Friction and seismic attenuation in rocks," *Nature*, **277**, pp. 528–531 (1979).

[18] D. Pasqualini, K. Heitmann, J.A. TenCate, S. Habib, D. Higdon, and P. A. Johnson, "Nonequilibrium and nonlinear dynamics in Berea and Fontainebleau sandstones: Low-strain regime," *J. Geophys. Res.*, **112**, B01204 (2007).

[19] Z. Chen and J. Qu, "Dislocation-induced acoustic nonlinearity parameter in crystalline solids," *J. Appl. Phys.*, **114**, 164906 (2013).

[20] D. N. Boccaccini and A. R. Boccaccini, "Dependence of Ultrasonic Velocity on Porosity and Pore Shape in Sintered Materials," *J. Nondestruct. Eval.*, **16**, pp. 187–192 (1997).

[21] S. Ekinci, "Characterisation of sintered metal products by using ultrasonics," *Insight*, **47**, pp. 674–677 (2005).

[22] J. A. Slotwinski, E. J. Garboczi, and K. M. Hebenstreit, "Porosity Measurements and Analysis for Metal Additive Manufacturing Process Control," *J. Res. Natl. Inst. Stan.*, **119**, pp. 494–548 (2014).

[23] A. S. Nowick and B. S. Berry, *Anelastic Relaxation in Crystalline Solids* (Academic, 1972).

[24] W. L. Johnson, S. A. Kim, G. S. White, and J. Herzberger, "Nonlinear resonant acoustic detection of cracks in multilayer ceramic capacitors," *2014 IEEE Ultrason. Symp. Proceedings* (Chicago, Sept. 3–6, 2014), pp. 248-251 (2014).